GEOPHYSICS, VOL. 85, NO. 2 (MARCH-APRIL 2020); P. O37–O45, 13 FIGS.
10.1190/GEO2018-0303.1

Seismic horizon picking by integrating reflector dip and instantaneous phase attributes

Yihuai Lou[1], Bo Zhang[1], Tengfei Lin[2], and Danping Cao[3]

ABSTRACT

Seismic horizons are the compulsory inputs for seismic stratigraphy analysis and 3D reservoir modeling. Manually interpreting horizons on thousands of vertical seismic slices of 3D seismic survey is a time-consuming task. Automatic horizon interpreting algorithms are usually based on the seismic reflector dip. However, the estimated seismic reflector dip is usually inaccurate near and across geologic features such as unconformities. We are determined to improve the quality of picked horizons using multiple seismic attributes. We assume that seismic horizons follow the reflector dip and that the same horizons should have similar instantaneous phase values. We first generate horizon patches using a reflector dip attribute, which is similar to current methods. We use seismic coherence attribute as the stop criteria for tracking the horizon within each patch. Considering the inaccuracy of reflector dip estimates at and near the discontinuous structures such as fault and unconformities, we use the seismic instantaneous phase attribute to improve the quality of the generated horizon patches. We generate horizons by merging the residual horizon patches and only outputting the best horizon in each iteration. Our method is capable of generating a horizon for each reflection within the 3D seismic survey, and the generated horizons strictly follow the seismic reflections over the whole seismic survey. Finally, each time sample of seismic traces is assigned a chronostratigraphic relative geologic time value according to the tracked horizons.

INTRODUCTION

Horizon interpretation is one of the key steps of locating reservoirs and well placement. Interpreters track horizon surfaces according to the amplitude, phase, and continuity patterns of seismic events. Horizon picking on a dense grid for a 3D seismic survey is a time-consuming task. Thus, automating the task will reduce the time consumption. There are four main categories for the automatic horizon-tracking methods.

The first category uses user-interpreted horizons to interpolate a set of separated horizons (Zeng et al., 1998). Unfortunately, the interpolated horizons usually cannot follow the local reflectors. The second category is the horizon patch method, which has two main steps. The first step is automatically tracking small horizon surfaces named horizon patches using seismic attributes on the user-defined subset of the seismic survey. The second step is merging the horizon patches to form the horizons. Borgos et al. (2003) first use peaks and troughs of the seismic amplitude to generate horizon patches and then merge the horizon patches to form a horizon by comparing the similarity of the waveforms of the patches. Monsen et al. (2007) merge the horizon patches by considering the waveform attributes and the topological relationships between the horizon patches. Verney et al. (2008) merge the horizon patches by considering the geometry relationship between horizon patches. The third category is based on the dip of the seismic reflectors. Lomask et al. (2006) first flatten the seismic reflection events using the reflector dip and then generate a relative geologic time (RGT) volume based on the flattened seismic volume. Luo and Hale (2013) first unfault a seismic image using fault slip vectors and then unfold the unfaulted image using seismic normal vectors (perpendicular to reflection events). Wu and Hale (2015) improve the stability of the horizon picking and compute a complete horizon volume with the constraint of sets of control points. The fourth category is based on unwrapping the instantaneous phase of the seismic data. Stark (2004) first unwraps the instantaneous phase of seismic data and then produces the RGT volume using the phase-unwrapped volume. Samples on

Manuscript received by the Editor 26 April 2018; revised manuscript received 2 November 2019; published ahead of production 26 November 2019; published online 30 January 2020.
[1]The University of Alabama, Department of Geological Science, Tuscaloosa, Alabama, USA. E-mail: ylou6@crimson.ua.edu; bzhang33@ua.edu.
[2]CNPC, Department of Middle East E&P, RIPED, Beijing, China. E-mail: lintf@petrochina.com.cn.
[3]China University of Petroleum (East China), School of Geoscience, Qingdao, China. E-mail: caodp@upc.edu.cn.

the same horizon should have the same RGT value. Wu and Zhong (2012) produce the RGT volume by using the graph-cut phase-unwrapping method. Unfortunately, unconformity surfaces have to be manually interpreted to constrain the phase unwrapping (Wu and Hale, 2015). Wu and Fomel (2018) compute horizons across faults by fitting, in least-squares sense, the horizons with local slopes and multigrid correlations of seismic reflections. Lou and Zhang (2018) use seismic amplitude, reflector dip, and instantaneous phase to track the horizons.

Selecting proper seismic attributes is very important for seismic interpretation, such as facies recognition, facies analysis, and structure interpretation (Zhang et al., 2014; Qi et al., 2016; Qi et al., 2018; Yuan et al., 2018; Lou et al., 2019). Common seismic attributes used for horizon tracking include seismic phases, reflector dip, and the peak or trough of the seismic amplitude. Guillon et al. (2013) use the convergence density of seismic reflection events to highlight periods of nondeposition. Dossi et al. (2015) use the cosine of the instantaneous phase to detect and characterize reflections in seismic and ground-penetrating radar data. Forte et al. (2016) use the cosine of the instantaneous phase to detect horizons. Unfortunately, seismic attributes, such as dip and unwrapped phase, are usually inaccurate at unconformities and near fault zones. Inaccurate seismic-attribute estimations could further introduce errors in the automatic horizon picking. The automatically tracked horizons may cross several seismic reflection events due to inaccurate seismic attributes. Another consideration in horizon tracking is that most of the current automatic horizon-tracking methods fail to consider the quality of the tracked horizons. The quality of automatically tracked horizons in areas with

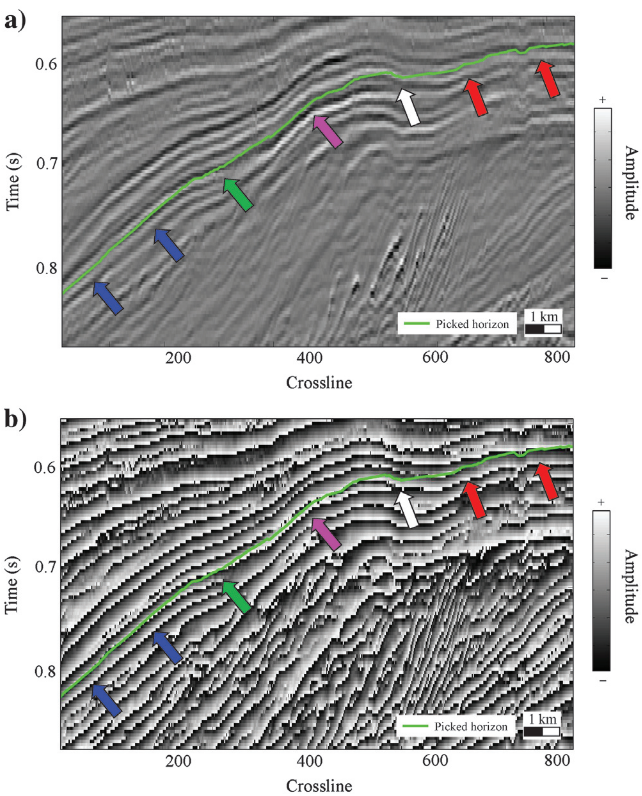

Figure 1. An automatic tracked horizon using the reflector dip overlaid on (a) a 2D inline seismic section and overlaid on (b) the corresponding 2D inline instantaneous phase section.

a high signal-to-noise ratio (S/N) is better than the quality of horizons tracked in noisy zones. Thus, it is better to track horizons with high quality and use the tracked horizons to guide the following automatic horizon-tracking procedures but the method currently does not work that way.

In this paper, we present a new method to iteratively track horizons using multiple seismic attributes and generate an RGT volume. We begin with tracking horizon patches using reflector dip. The tracked horizon patches stop at potential faults or unconformities by considering the coherence of samples. We next improve the accuracy of the horizon patches by using instantaneous phase. We finally build the horizon and the RGT volume by merging different horizon patches into single horizons throughout the seismic survey. We illustrate our workflow step by step by testing it on poststack seismic survey acquired in Block F3 (offshore Netherland). The F3 block seismic data survey consists of 350 inline and 825 crossline seismic sections. The inline and crossline interval is 25 m and the time sampling interval is 4 ms.

METHOD

Seismic attributes such as reflector dip and instantaneous phase are used for automatic horizon-picking algorithms. Figure 1a shows an automatically tracked horizon (the green line) overlaid with a 2D inline vertical slice of the poststack seismic amplitude. Figure 1b shows the same tracked horizon shown in Figure 1a overlaid with a 2D inline vertical slice of the instantaneous phase seismic attribute. We obtain the instantaneous phase seismic attribute from the poststack seismic data shown in Figure 1a. The reflector dip seismic attribute is used as the input for the automatic horizon picking. The green and white arrows indicate two observable unconformity locations. Note that the automatically tracked horizon follows the seismic reflections on both sides of the unconformity locations. The blue arrows indicate the left side of the unconformity location indicated by the green arrow. The purple arrow indicates the right side of the unconformity location indicated by the green arrow (the left side of the unconformity location indicated by the white arrow). The red arrows indicate the right side of the unconformity location indicated by the white arrow. However, the tracked horizon crosses two seismic reflections at the unconformity locations.

We propose a four-step workflow to track horizons by integrating multiple seismic attributes (Figure 2) to overcome the aforementioned automatic horizon-picking challenge. We begin by defining the size of horizon patches and seeds. We use the seeds as the constraints for the horizon patches (Wu and Hale, 2015), which follow the local reflector dip. Considering that the dip estimation is usually inaccurate near the discontinuous zones, such as unconformities and faults, we refine the horizon patches using instantaneous phase. We then merge horizon patches into horizons, based on their topological relationship. We rank all merged horizons and only output the best horizon, iteratively. We output the best horizon in every iteration, and horizon patches that belong to the outputted horizon are excluded from the following horizon patches-merging process. We repeat the process of merging, ranking, and outputting until all the horizon patches belong to a certain horizon.

Step one: Patch size and seed definition

The patch size varies according to the S/N and the complexity of the structure of the study area. We consider the following criteria in the determination of the size of horizon patches. The patch size should be small enough to ensure that the tracked patches strictly follow the local reflector dip. The defined patches overlap to facilitate the following process of patch merging. The topological relationship of the tracked horizon patches within the overlapping zone is used to avoid the crossing phenomenon in the merging process of horizon patches. The user-defined patch size of our study case is 36 crossline × 18 inline seismic sections. The size of the overlapping zone is six crossline by three inline sections. Figure 3 shows defined overlapping patches for our seismic survey where the red rectangles are the defined horizon patches and the blue strips are the overlapping zones between defined horizon patches. Every patch is overlapped with four nearby patches, except patches along the border. Seismic traces used for the seeds generation (the black dots in Figure 3) are located at the center of the corresponding horizon patches. We select the peaks and troughs of the selected seismic traces as the seeds constraining the generation of horizon patches. Figure 4 shows defined seeds on a representative inline seismic section.

Step two: Horizon patches generation and refinement

Each defined seed is the constraint for the horizon patch generation. We use the following three criteria to generate the horizon patches. First, the horizon patches have to follow the local reflector dip. Second, the horizon patches pass the corresponding seeds. Third, the horizon patches stop at the samples if the coherence value of these samples is below a user-defined coherence threshold. Then, the horizon patches generation becomes a constrained optimized problem (Wu and Hale, 2015).

We arrange the two-way traveltime (TWT) of the samples in the patch in a vector format:

$$\boldsymbol{\beta} = (\beta_1, \beta_2, \ldots, \beta_{m*n}), \tag{1}$$

where m and n are the patch sizes along the inline and crossline direction, respectively. Then, the constrained optimization problem can be described as

$$\text{minimize } S(\boldsymbol{\beta}) = \sum_{i=1}^{m\times n} |\Delta\mathbf{t}_i^{(\beta)} - \Delta\mathbf{t}_i^{(\mathrm{Seis})}|^2 \tag{2a}$$

$$\text{subject to } \beta_s = t_0(\text{seed}), \tag{2b}$$

where $t_0(\text{seed})$ is the TWT of the seed and $\Delta\mathbf{t}_i^{(\beta)}$ and $\Delta\mathbf{t}_i^{(\mathrm{Seis})}$ are the dips computed from the tracked horizon patch and the dips computed from seismic reflection events, respectively:

$$\Delta\mathbf{t}_i^{(\beta)} = \begin{bmatrix} \beta_{i+m} - \beta_i \\ \beta_{i+1} - \beta_i \end{bmatrix}, \tag{3}$$

$$\Delta\mathbf{t}_i^{(\mathrm{Seis})} = \begin{bmatrix} p \\ q \end{bmatrix}. \tag{4}$$

The TWT of the selected seed is regarded as the constraint point. The p and q are the inline and crossline dips computed from seismic events in the format of dt. Because the TWT of samples in the patch is in a vector format, $\beta_{i+m} - \beta_i$ and $\beta_{i+1} - \beta_i$ represent the inline and crossline dips computed from tracked horizon patches in the format of dt. Our purpose is to minimize the difference between the dips computed from tracked horizon patches and the dips computed from seismic events. We use the constrained Gaussian-Newton method (Doicu et al., 2002) to solve the constrained optimization problem shown in equation 2. The size of the tracked horizon patches is affected by the continuity of the seismic reflection events. The threshold used for stopping the horizon patches tracking is 0.3 in our testing. Figure 5a and 5b shows one representative horizon patch before and after "trimming" according to the coherence value of the samples on the horizon patch, respectively.

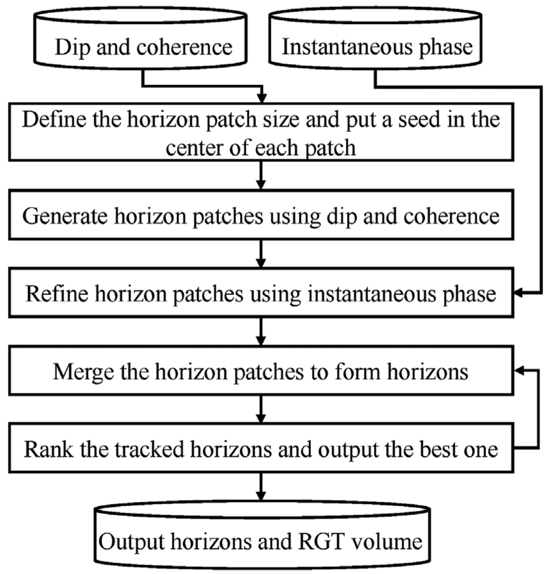

Figure 2. Flowchart showing the automatic horizon tracking and chronostratigraphic RGT volume generation based on seismic attributes.

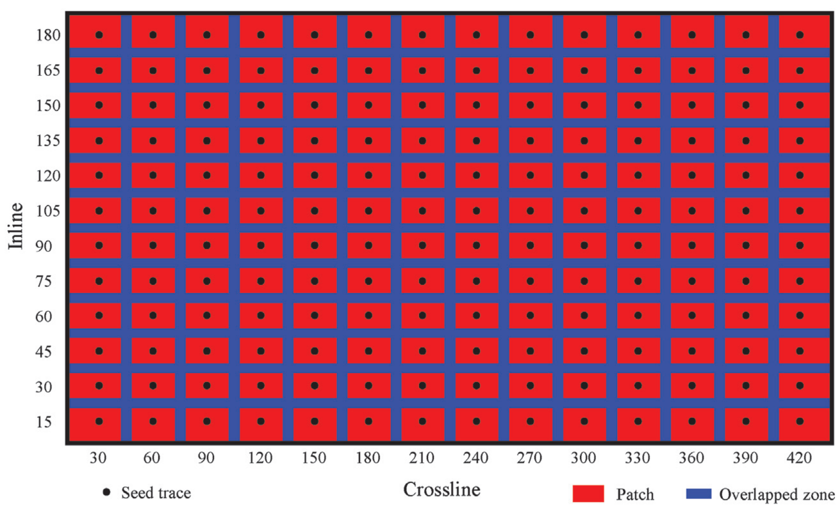

Figure 3. The defined overlapping horizon patches.

All the tracked horizon patches form the horizon patch bank used for merging. Figure 6a shows the tracked horizon patches overlaid on a representative inline instantaneous phase section. The red and yellow horizon curves are the horizon patches passing through peaks and troughs of the seismic traces, respectively. We call the horizon patches trough patches if the corresponding constraint seeds are located at the troughs of the seismic traces and peak patches if the corresponding constraint seeds are located at the peaks of the seismic traces. The seismic sections numbered 1 and 2 in Figure 6c illustrate the magnified horizon patches located in the red and blue rectangles shown in Figure 6a, respectively. The tracked horizon patches illustrate that the horizon patches fail to follow the local reflectors near the unconformity. Furthermore, the instantaneous phase has an abrupt change along the unconformity surface.

We next refine the horizon patches using the instantaneous phase attribute. We “reshape” the trough and peak horizon patches by shifting the TWT on patches so that the samples of the horizon patches have the same instantaneous phase value. We do not shift the TWT for the constraint seed. We shift all of the other samples on the horizon patch to pass the same instantaneous phase value as that of the constraint seed. The vertical search window is one period of the local instantaneous phase. Figure 6b shows the refined horizon patches overlaid on the same instantaneous phase inline section. The seismic sections numbered 3 and 4 in Figure 6c illustrate

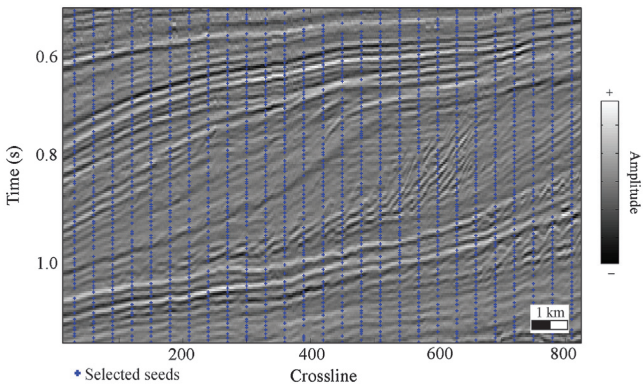

Figure 4. The defined seeds (the blue crosses) on a representative inline section.

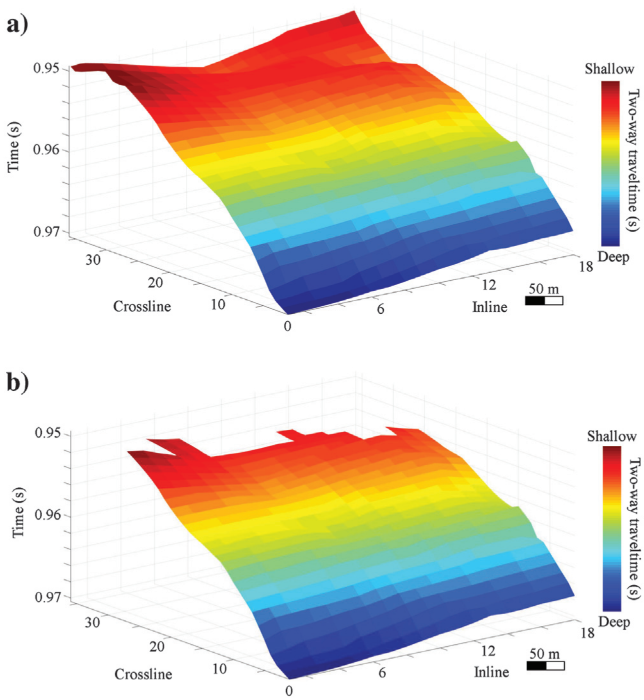

Figure 5. One representative horizon patch (a) before and (b) after trimming according to the coherence value of the samples on the horizon patch. The t_0 represents the two-way traveltime of samples on the patch.

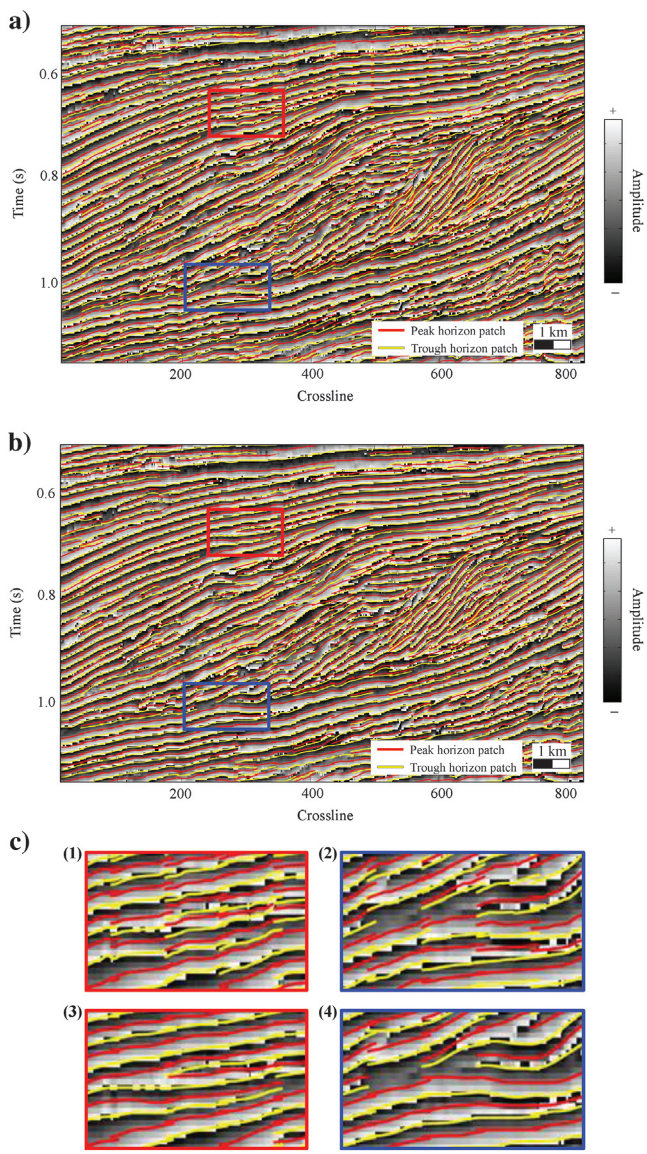

Figure 6. (a) The tracked horizon patches overlaid on the representative inline instantaneous phase section. (b) The refined horizon patches overlaid on the same inline instantaneous phase section. (c) The magnified tracked horizon patches from the red and blue rectangles in (a and b). Seismic sections 1 and 2 are indicated by the red and blue rectangles in (a), respectively. Seismic sections 3 and 4 are indicated by the red and blue rectangles in (b), respectively.

the magnified horizon patches located in the red and blue rectangles shown in Figure 6b, respectively. Note that the refined horizon patches strictly follow the local reflectors and the instantaneous phase.

Step three: Horizon-patch merging

We assign each tracked horizon patch a rank value according to the average coherence value of all the samples on the patch. The horizon patches merging starts with the horizon patch that has the highest rank value. The patch with the highest rank value (the gray patch in Figure 7a) serves as the target patch. The peak/trough patches around the target patch serve as the candidate-merging patches (the red rectangles in Figure 7a). The trough patch only merges with surrounding trough patches, and the peak patch only merges with surrounding peak patches. We do not allow a trough patch passing across two merged peak patches and vice versa. We only merge one candidate patch each time that has the best match with the target patch.

The seismic traces within the overlapping zone have two tracked TWT (t_0^a and t_0^b). The first tracked t_0^a belongs to the target patch, whereas the second t_0^b belongs to the candidate patch. We define the matching degree by comparing the similarity S between the seismic amplitude within the overlapping zone of the target patch and candidate patches. We denote the seismic trace within the overlapping zone as $f(i,j)$, where (i,j) is the location axis of the seismic trace. The seismic amplitudes centered at t_0^a and t_0^b are defined $f_a(i,j)$ and $f_b(i,j)$, respectively. Then, the similarity between these two seismograms is defined as

$$S(i,j)=\frac{\sum_{k=-K}^{+K}\{[f_a(\tau_0^a+k,i,j)+f_b(\tau_0^b+k,i,j)]^2+[f_a^{\mathrm{H}}(\tau_0^a+k,i,j)+f_b^{\mathrm{H}}(\tau_0^b+k,i,j)]^2\}}{\sum_{k=-K}^{+K}\{[f_a(\tau_0^a+k,i,j)]^2+[f_a^{\mathrm{H}}(\tau_0^a+k,i,j)]^2+[f_b(\tau_0^b+k,i,j)]^2+[f_b^{\mathrm{H}}(\tau_0^b+k,i,j)]^2\}}, \tag{5}$$

where K is the half-window size in number of samples, τ_0^a and τ_0^b are the time indices corresponding to t_0^a and t_0^b, respectively, and f^H is the Hilbert-transform component of the real seismic trace f. Then, the similarity between the target and candidate patches is defined as

$$S=\frac{\sum_{i=1}^{I}\sum_{j=1}^{J}S(i,j)}{I*J}, \tag{6}$$

where I and J are the length and width of overlapping zones of the patches along the inline and crossline directions, respectively.

After the target path (the gray patch in Figure 7a) merges the candidate-merging patch with the highest similarity, the new merged horizon patch serves as the target patch and the surrounding patches serve as the candidate-merging patches. We suppose that each horizon covers the entire seismic survey, and our merging process continues until our merged horizon patches cover the whole seismic survey. Figure 7b shows the final merged horizon patches. The white zones indicated by the black arrows in Figure 7b are patches that have very low waveform similarity between the candidate patch and the target patch. Figure 7c shows the interpolated horizon across the seismic survey. We treat the interpolated horizon as the first tracked horizon within our seismic survey.

We again select the patch with the highest rank value as the target patch and repeat the merging process. The used horizon patches are excluded when we select the best horizon patch in the current merging iteration. In other words, the used horizon patches cannot be used as the first target horizon patch in each merging loop. In this manner, we avoid using the same horizons in different merging loops. However, these used patches can be used as candidates for all the merging loops. Figure 8 shows all the merged horizons and interpolated horizons overlaid on the representative inline seismic section. The yellow and dashed red curves in Figure 8 are the original merged part and interpolated part of the horizons, respectively. Note that some of the interpolated parts of the horizons cross several seismic events (Figure 8). We next analyze whether we should preserve the interpolated part of the horizons.

The horizons should not cross each other after the geometry-analysis process. Figure 9 illustrates how we analyze the geometry relationship between two crossing horizons. There are two cases in

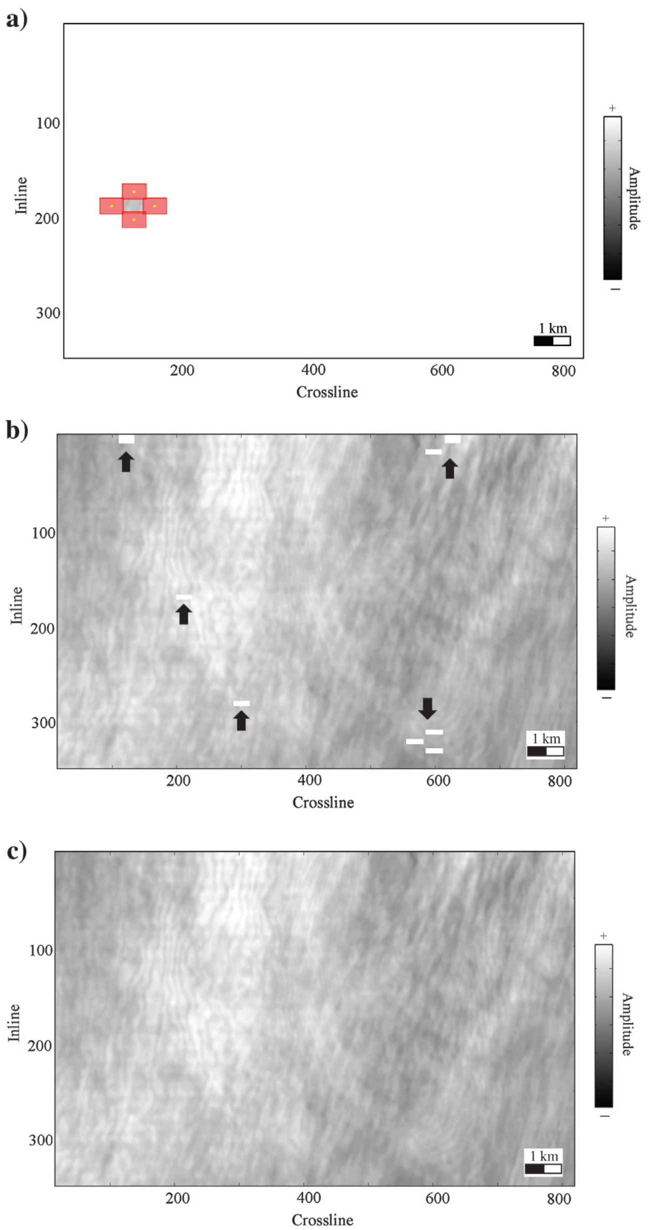

Figure 7. (a) The target patch and nearby candidate patches before merging any candidate patches. (b) The merging result after merging all of the candidate patches. (c) The interpolated horizon across the seismic survey.

our geometry analysis. Two peak horizons or two trough horizons merge together at one end due to the reflections from nonconformity (Figure 9a). The dashed red and yellow curves in Figure 9a are two horizons overlaid on one representative inline seismic section. We first detect the crossing point (the red arrow in Figure 9a) between two crossing horizons. The black rectangle in Figure 9a is the analysis window centered at the crossing point. Figure 9b shows another case after the merging and interpolation processes, where the dashed red horizon overlaps with the yellow horizon on both sides. We only analyze the left and right beginning crossing points if there are multiple crossing points for two horizons in an inline or crossline section (Figure 9b).

We analyze the local horizon "trend" to determine which horizon wins the part beyond the crossing point in this analysis window. We suppose that the interpreted horizons should have a gradual variation of TWT if there is no fault cutting through the interpreted horizon. We use the variance of the derivative of the TWT of the tracked horizons within the analysis window to evaluate the accuracy of the horizon near the crossing zone. Each sample on the horizon has inline derivative, t'_{inline}, and crossline derivative, $t'_{\mathrm{crossline}}$, of the TWT:

$$t'_{\mathrm{inline}} = t_0(i+1,j) - t_0(i,j), \tag{7}$$

$$t'_{\mathrm{crossline}} = t_0(i,j+1) - t_0(i,j), \tag{8}$$

where i and j are the inline and crossline indices, respectively. The variance of the derivative σ within the analysis window is defined as

$$\sigma^2 = \frac{1}{2}\frac{\sum_{i=1}^{O}\sum_{j=1}^{P}(t'_{\mathrm{inline}} - \mu_{\mathrm{inline}})^2}{O \times P} + \frac{1}{2}\frac{\sum_{i=1}^{O}\sum_{j=1}^{P}(t'_{\mathrm{crossline}} - \mu_{\mathrm{crossline}})^2}{O \times P}, \tag{9}$$

$$\mu_{\mathrm{inline}} = \frac{\sum_{i=1}^{O}\sum_{j=1}^{P} t'_{\mathrm{inline}}}{O \times P}, \tag{10}$$

$$\mu_{\mathrm{crossline}} = \frac{\sum_{i=1}^{O}\sum_{j=1}^{P} t'_{\mathrm{crossline}}}{O \times P}, \tag{11}$$

where O and P are the numbers of crossing points along the inline and crossline directions, respectively. The horizon with larger derivative variance indicates a high fluctuation of the tracked horizon, thus a lower quality of the tracked horizon. The horizon with smaller derivative variance indicates a low fluctuation of the tracked horizon, thus a relatively higher quality of the tracked horizon. We use this strategy to analyze the geometry relationship between crossing-cut horizons

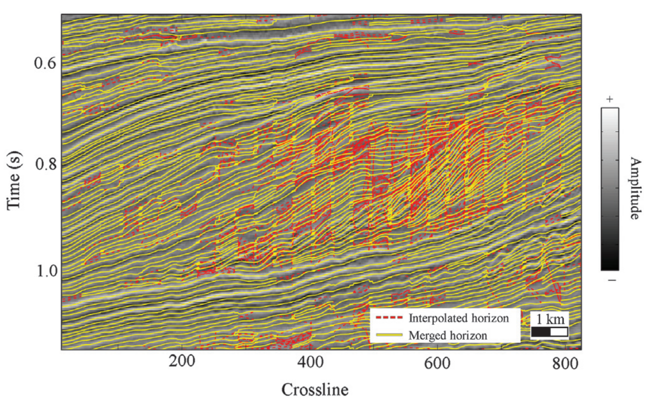

Figure 8. All merged and interpolated horizons overlaid on the representative inline seismic section.

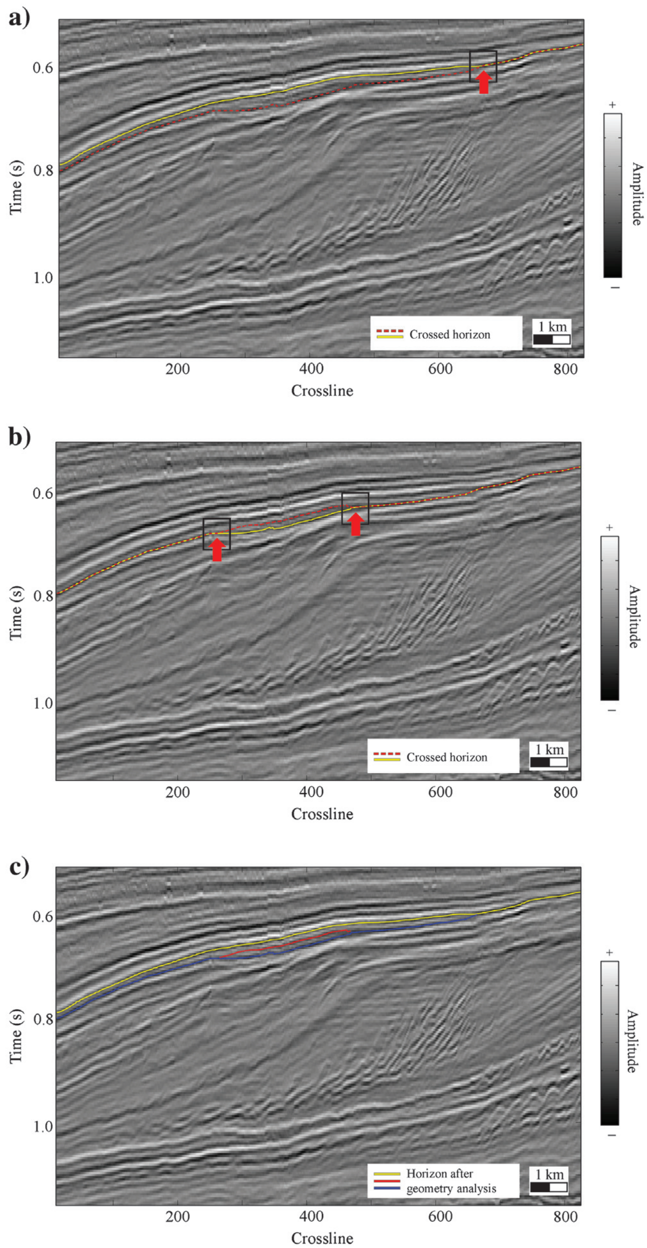

Figure 9. Geometry analysis between merged and interpolated horizons. (a) Two trough horizons merge together at one end due to the reflections from a nonconformity. (b) Two trough horizons merge together at both ends. (c) The result of three horizons after the geometry analysis.

for every inline and crossline. Figure 9c shows the results of the three horizons overlaid on the representative inline seismic section after cutting the crossing parts. Figure 10a and 10b illustrates the two horizons in the 3D view before and after the process of geometry analysis, respectively. The white arrow in Figure 10a indicates that two horizons cross at the end before the geometry analysis. We then use equations 7–11 to analyze the derivative variance of these two crossing horizons. The pink horizon has a lower derivative variance, which indicates higher overall quality. Thus, the pink horizon wins the crossing part indicated by the white arrow in Figure 10b. Figure 11a shows all the tracked horizons (the yellow and red lines) overlaid on one representative inline section after the geometry analysis. The yellow and red lines in Figure 11a are the selected horizon and invalid horizons, respectively. We next explain how to select the best horizon from all of the tracked horizons in step four.

Step four: Horizon ranking and output

We define a score to judge the quality of the tracked horizons. The score of the horizons considers the average semblance, which is calculated by applying an analysis window centered at the horizon, and the ratio between the merged zones over the interpolated zone. For simplicity, the average semblance and the ratio have the same weight. We calculate the semblance C for every horizon using the semblance-based coherence (Marfurt et al., 1998):

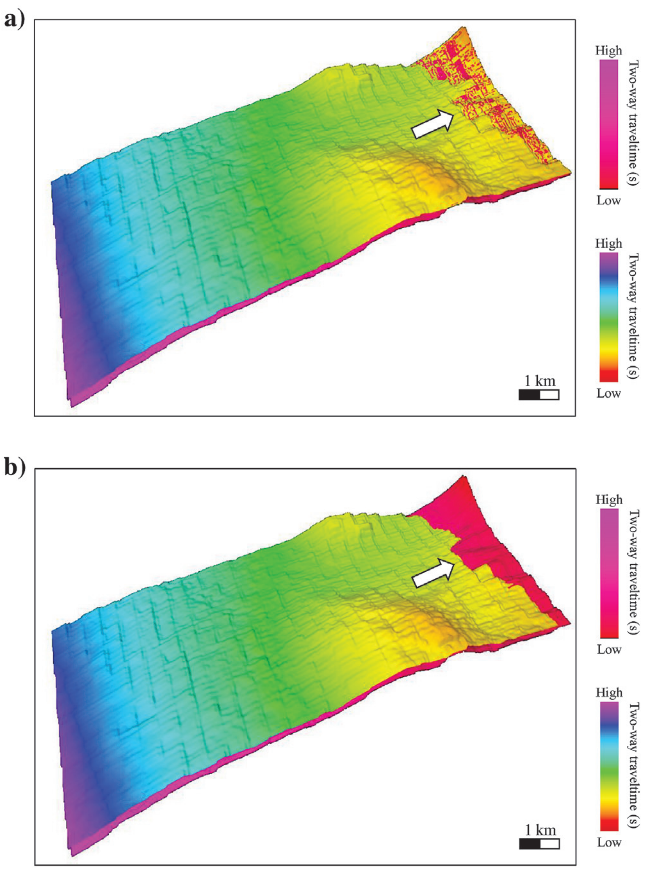

Figure 10. The 3D view of two crossing horizons (a) before and (b) after horizon geometry analysis.

$$C(i,j)=\frac{\sum_{k=-K}^{+K}\{[\sum_{i=1}^{R}\sum_{j=1}^{Q}f(\tau_0+k,i,j)]^2+[\sum_{n=1}^{R}\sum_{j=1}^{Q}f^{\mathrm{H}}(\tau_0+k,i,j)]^2\}}{R\times Q\sum_{k=-K}^{+K}\sum_{i=1}^{R}\sum_{j=1}^{Q}\{[f(\tau_0+k,i,j)]^2+[f^{\mathrm{H}}(\tau_0+k,i,j)]^2\}}, \tag{12}$$

$$C_{\mathrm{ave}}=\frac{\sum_{l=1}^{L}C(i,j)}{L}, \tag{13}$$

where i and j are the inline and crossline indexes, respectively; $\tau_0(i,j)$ is the TWT of the horizon at location (i,j); $f(\tau_0,i,j)$ is the seismic amplitude; K is the size of the vertical window used for the semblance calculation; R and Q are the sizes of the horizontal windows used for the semblance calculation along inline and crossline direction, respectively; f^{H} is the Hilbert-transformed component of the real seismic trace, f; L is total number of seismic traces on the tracked horizon; and C_{ave} is the average semblance value of the analyzed horizon. Then, the score of the tracked horizon is defined as

$$HC=C_{\mathrm{ave}}+\frac{A_m}{A_i+A_m}, \tag{14}$$

where A_m and A_i are the areas of the merged and interpolated part of the horizon, respectively. We treat the horizon with the highest score as our first final automatically tracked horizon (the yellow line in Figure 11a), and we treat the other merged horizons as invalid hori-

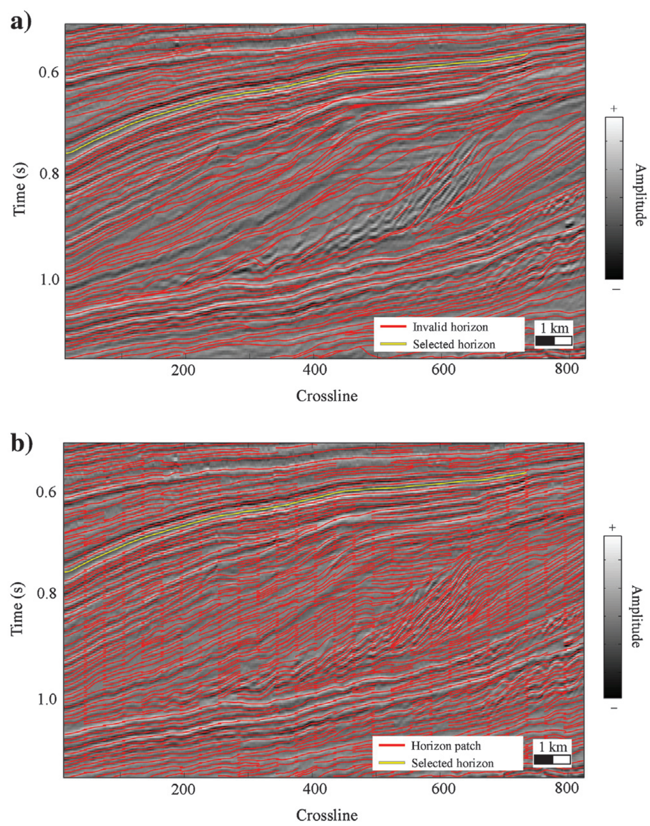

Figure 11. (a) All of the merged horizons after geometry relationship analysis overlaid on the representative inline seismic section. The merged horizons are classified as the selected horizon and invalid horizons. (b) The first output horizon (the yellow line) and remaining horizon patches (the red curves).

zons (the red lines in Figure 11a). The new horizon patch bank includes all of the horizon patches (the red curve in Figure 11b) except those used by our first final tracked horizon. We then repeat the merging and ranking processes to find the next best horizon until all of the horizon patches are used. Figure 12 shows the final result after we merge all the remaining horizon patches. The yellow lines and red numbers in Figure 12 are tracked horizons and their corresponding RGT values, respectively. The minimum and maximum values of RGT are 100 and 1200, respectively. However, these are relative values that can be redefined by the user. We determine the RGT value of each horizon according to the maximum TWT of the horizons. We next interpolate the RGT values for all samples of the seismic volume using the assigned RGT on the tracked horizons. Figure 13a and 13b shows the computed RGT of one representative inline section and RGT volume in a chair display using the automatically tracked horizons.

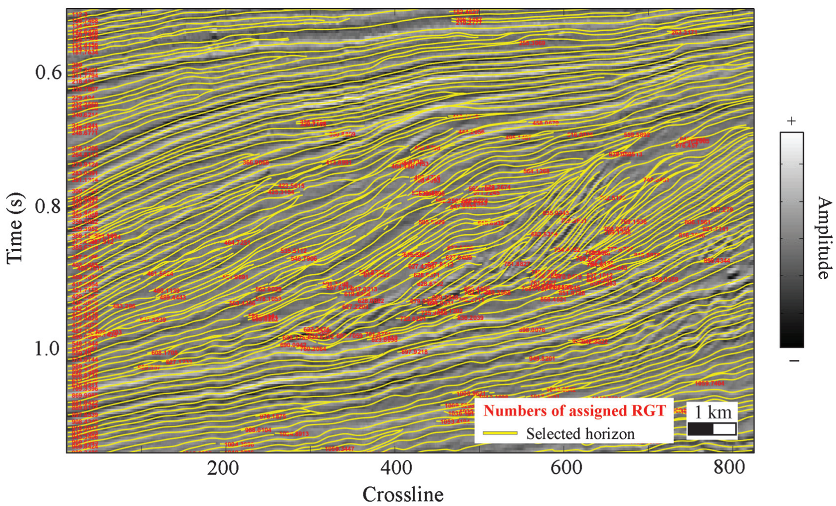

Figure 12. The final outputted horizons with the assigned RGT value.

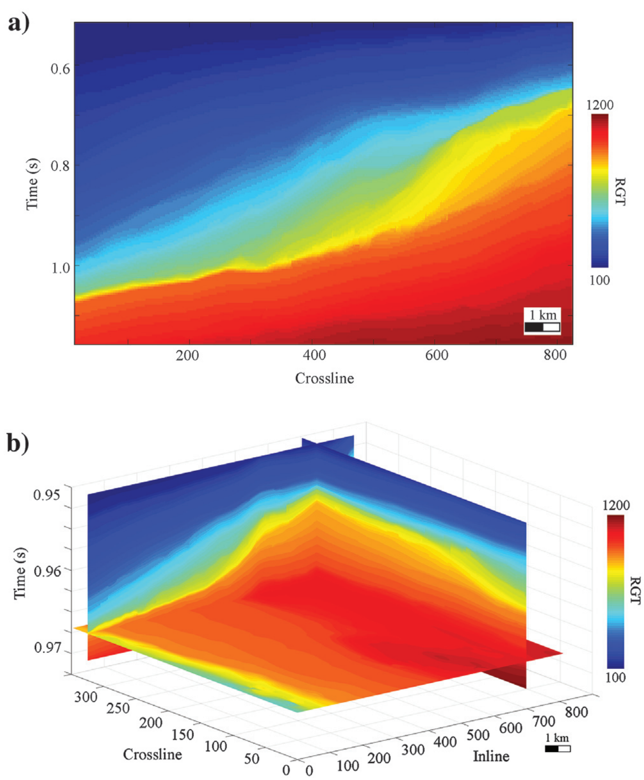

Figure 13. (a) The computed RGT of the representative inline section. (b) The chair display of the RGT volume using automatically tracked horizons.

DISCUSSION

Our method is based on two assumptions: (1) Seismic horizons should follow the reflector dip, and (2) the same horizon should have similar instantaneous phase values. Both assumptions have been used to develop algorithms for automated horizon picking. We combine those two assumptions together for the first time to pick seismic horizons. The value of the instantaneous phase attribute can easily be affected by the noise. Thus, we suggest applying a structure-oriented filtering to the seismic data before computing the seismic instantaneous phase, reflector dip, and coherence attributes. Tracking horizons within a small subdivided seismic survey (patch) improves the accuracy of the tracked horizons and heavily reduces the size of the matrices needed in the optimization process. Our algorithm assumes that the tracked horizon patches after the refinement process accurately follow the seismic reflections. Thus, the time cost of horizon patch tracking is the same as for the currently used methods. To make sure that the merged horizons follow seismic reflections, we only output the best merged horizon in each horizon-merging iteration and the best merged horizon functions as constraints in the following iterations of horizon patches merging process. Merging the horizon patches iteration by iteration is the most time-consuming step. The main reason why we need an iterative process is that we do not have prior information about which seismic reflections will be the "best" reflection in current horizon-tracking iteration. One possible solution of expediting this process is to first rank the priority of each seismic reflection using signal comparison algorithms such as dynamic time warping (Sakoe and Chiba, 1978).

A proper horizon patch size and low coherence threshold are the parameters needed for the generation of horizon patches. The patch size in our application is 36 crosslines × 18 inlines. We acknowledge that it is challenging to link the patch size with the parameters of a seismic survey or seismic data itself. We suggest a two-step workflow to determine the patch size. The first step is generating the horizon patches according to a set of user-defined patch sizes. The second step is using human judgment to examine whether the generated horizon patches follow well the local seismic reflections. We choose the largest size whose corresponding horizon patches follow the local reflections as the patch size in our workflow. We again determine the low coherence threshold through testing. We choose 0.3 as the low coherence threshold to stop the horizon-tracking process within the defined patch at fault locations. A low similarity value is needed to determine whether two horizon patches should be merged in the patch-merging process. The value of low similarity is set as the same value as the low-coherence threshold used in the horizon patch-generating process.

Picking horizons across faults would be a challenge for our method. Our method is designed to minimize two objectives: (1) the difference between the dip computed from picked horizons and dip computed using seismic waveforms and (2) the phase difference on the picked horizons between nearby seismic traces. However, the dip of picked horizons at the fault location is infinite and the dip computed using seismic waveform is inaccurate at the fault location. The infinite dip and inaccurate dip may hinder us to accurately tracking the horizons across the faults. One solution is to stop the horizon tracking at the fault location and then align the horizon patches across the faults using algorithms such as dynamic time programming (Sakoe and Chiba, 1978).

CONCLUSION

Most current horizon-picking methods only use one seismic attribute, such as the reflector dip or instantaneous phase, as the input to automatically track horizons. The application demonstrates that the tracked horizon that only used one seismic attribute (reflector dip) may cross several seismic reflections at unconformity locations. Inaccurate computed dip values are responsible for inaccurate horizon picking at the unconformity locations. We proposed to stabilize the horizon picking at the unconformity locations using multiple seismic attributes (coherence, reflector dip, and instantaneous phase). Interpreters usually produce seismic horizons by following the peaks or troughs of reflections. Thus, we selected peaks and troughs of seismic reflections as seeds to constrain the horizon patch-generation process. The constrained Gaussian-Newton method is used by our algorithm to make sure that the generated horizon patches pass through the selected seeds. We tested our method on field poststack seismic survey data. We noticed that the same horizon has almost the same instantaneous phase values across the whole seismic survey. Thus, we successfully corrected the inaccurate two-way traveltime of picked horizon patches in the process of horizon patch generation by using the instantaneous phase attribute. The refined horizons patches follow very well with the poststack seismic reflections not only at locations where we have parallel and continuous reflections but also at unconformity locations where the dip attribute is inaccurate. It is very common that we have very good S/N for some seismic reflections and low S/N for other seismic reflections even within the same seismic survey. Thus, it would be beneficial to first pick the seismic reflections with high S/N and then use those picked horizons as the constraints for the following horizon-picking process. Unfortunately, only picking one horizon each iteration would increase the computation cost of automatic horizon-picking algorithms.

ACKNOWLEDGMENTS

The authors thank the Netherlands Organization for Applied Scientific Research (TNO) for allowing the seismic data used in this paper to be public.

DATA AND MATERIALS AVAILABILITY

Data associated with this research are available and can be accessed via the following URL: https://wiki.seg.org/wiki/Open_data.

REFERENCES

Borgos, H. G., T. Skov, T. Randen, and L. Sonneland, 2003, Automated geometry extraction from 3D seismic data: 73rd Annual International Meeting, SEG, Expanded Abstracts, 1541–1544, doi: 10.1190/1.1817590.
Doicu, A., F. Schreier, and M. Hess, 2002, Iteratively regularized Gauss-Newton method for bound-constraint problems in atmospheric remote sensing: Computer Physics Communications, **153**, 59–65, doi: 10.1016/S0010-4655(03)00138-3.
Dossi, M., E. Forte, and M. Pipan, 2015, Automated reflection picking and polarity assessment through attribute analysis: Theory and application to synthetic and real GPR data: Geophysics, **80**, no. 5, H23–H35, doi: 10.1190/geo2015-0098.1.
Forte, E., M. Dossi, M. Pipan, and A. D. Ben, 2016, Automated phase attribute-based picking applied to reflection seismics: Geophysics, **81**, no. 2, V141–V150, doi: 10.1190/geo2015-0333.1.
Guillon, S., N. Keskes, J. Gallon, and M. Donias, 2013, Geotime: A 3D automatic tool for chronostratigraphic seismic interpretation and filtering: The Leading Edge, **32**, 154–159, doi: 10.1190/tle32020154.1.
Lomask, J., A. Guitton, S. Fomel, J. Claerbout, and A. A. Valenciano, 2006, Flattening without picking: Geophysics, **71**, no. 4, P13–P20, doi: 10.1190/1.2210848.
Lou, Y., and B. Zhang, 2018, Automatic horizon picking using multiple seismic attributes: 88th Annual International Meeting, SEG, Expanded Abstracts, 1683–1687, doi: 10.1190/segam2018-2997698.1.
Lou, Y., B. Zhang, R. Wang, T. Lin, and D. Cao, 2019, Seismic fault attribute estimation using a local fault model: Geophysics, **84**, no. 4, O73–O80, doi: 10.1190/geo2018-0678.1.
Luo, S., and D. Hale, 2013, Unfaulting and unfolding 3D seismic images: Geophysics, **78**, no. 4, O45–O56, doi: 10.1190/geo2012-0350.1.
Marfurt, K. J., R. L. Kirlin, S. L. Farmer, and M. S. Bahorich, 1998, 3-D seismic attributes using a semblance-based coherency algorithm: Geophysics, **63**, 1150–1165, doi: 10.1190/1.1444415.
Monsen, E. M., H. G. Borgos, P. L. Guern, and L. Sonneland, 2007, Geologic-process-controlled interpretation based on 3D Wheeler diagram generation: 77th Annual International Meeting, SEG, Expanded Abstracts, 885–889, doi: 10.1190/1.2792549.
Qi, J., T. Lin, T. Zhao, F. Li, and K. Marfurt, 2016, Semisupervised multiattribute seismic facies analysis: Interpretation, **4**, no. 1, SB91–SB106, doi: 10.1190/INT-2015-0098.1.
Qi, J., B. Lyu, A. AlAli, G. Machado, Y. Hu, and K. J. Marfurt, 2018, Image processing of seismic attributes for automatic fault extraction: Geophysics, **84**, no. 1, O25–O37, doi: 10.1190/geo2018-0369.1.
Sakoe, H., and S. Chiba, 1978, Dynamic programming algorithm optimization for spoken word recognition: IEEE Transactions on Acoustics, Speech, and Signal Processing, **26**, 43–49, doi: 10.1109/TASSP.1978.1163055.
Stark, T. J., 2004, Relative geologic time (age) volumes-relating every seismic sample to a geologically reasonable horizon: The Leading Edge, **23**, 928–932, doi: 10.1190/1.1803505.
Verney, P., M. Perrin, M. Thonnat, and J. F. Rainaud, 2008, An approach of seismic interpretation based on cognitive vision: 70th Annual International Conference and Exhibition Incorporating SPE EUROPEC, EAGE, Extended Abstracts, doi: 10.3997/2214-4609.20147604.
Wu, X., and S. Fomel, 2018, Least-squares horizons with local slopes and multi-grid correlations: Geophysics, **83**, no. 4, IM29–IM40, doi: 10.1190/geo2017-0830.1.
Wu, X., and D. Hale, 2015, Horizon volumes with interpreted constraints: Geophysics, **80**, no. 2, IM21–IM33, doi: 10.1190/geo2014-0212.1.
Wu, X., and G. Zhong, 2012, Generating a relative geologic time volume by 3D graph-cut phase unwrapping method with horizon and unconformity constraints: Geophysics, **77**, no. 4, O21–O34, doi: 10.1190/geo2011-0351.1.
Yuan, S., Y. Su, T. Wang, J. Wang, and S. Wang, 2018, Geosteering phase attributes: A new detector for the discontinuities of seismic images: IEEE Geoscience and Remote Sensing Letters, **99**, 1–5, doi: 10.1109/LGRS.2018.2866419.
Zeng, H., M. M. Backus, K. T. Barrow, and N. Tyler, 1998, Stratal slicing — Part 1: Realistic 3-D seismic model: Geophysics, **63**, 502–513, doi: 10.1190/1.1444351.
Zeng, H., S. C. Henry, and J. P. Riola, 1998, Strata slicing — Part 2: Real 3-D seismic data: Geophysics, **63**, 514–522, doi: 10.1190/1.1444352.
Zhang, B., Y. Liu, M. Pelissier, and N. Hemstra, 2014, Semiautomated fault interpretation based on seismic attributes: Interpretation, **2**, no. 1, SA11–SA19, doi: 10.1190/INT-2013-0060.1.